Wall-Modeled Large Eddy Simulations of the DLR LK6E2 Airframe

Jordan B. Angel*, Aditya S. Ghate, Gaetan K. W. Kenway, Man Long Wong, and Cetin C. Kiris
Volcano Platforms Incorporated, Palo Alto, CA 94304, USA

Wall-modeled large eddy simulations (WMLES) of the DLR LK6E2 generic missile airframe are performed over an angle-of-incidence range $13^\circ \leq \sigma \leq 19^\circ$ at Mach 0.85 and roll angle $\lambda = 45^\circ$, using the GPU-native compressible Navier–Stokes solver Volcano ScaLES on a Cartesian–octree mesh. The sweep extends prior work to lower incidence angles in order to resolve the weaker secondary break in rolling moment near $\sigma = 14^\circ$, in addition to the primary break near $\sigma = 16^\circ$. Predicted rolling-moment coefficients show good agreement with DLR HST/TWG wind-tunnel measurements across the full range, including the secondary-break regime. Both breaks are captured and attributed to a common physical mechanism involving progressive weakening and eventual disappearance of the leading normal shock on the port horizontal wing, accompanied by growth of an outboard separated region and reorganization of the associated vortex system. A per-wing decomposition indicates that the secondary break is dominated by a local change in the contribution of this wing, with the kink in the integrated rolling moment concentrated over $\sigma \in [13.5^\circ, 14.5^\circ]$, while the remaining wings exhibit nearly constant trends. Power spectral densities of pressure at numerical probes are compared against scale-resolving simulations at matched probe locations and operating conditions, enabling direct assessment of unsteady surface pressure content across methods.

Nomenclature

C_l	=	rolling moment coefficient
d_{ref}	=	reference body diameter, $d_{\mathrm{ref}} = 0.05$ m
f	=	frequency, Hz
f_s	=	probe-output sampling rate, Hz
f_{Nyq}	=	Nyquist frequency, $f_s/2$
h	=	finest isotropic Cartesian cell size in the body region
M_∞	=	freestream Mach number
N_{samples}	=	number of samples retained in the statistically stationary window
N_{seg}	=	number of Welch segments
p_∞	=	freestream static pressure
SEM	=	standard error of the mean
T_∞	=	freestream static temperature
$T^\star$	=	record span in convective time units, $T^\star = N_{\mathrm{samples}}\,\Delta t_{\mathrm{samp}}/\mathrm{CTU}$
t	=	physical time
$t^\star$	=	convective time, $t^\star = t/\mathrm{CTU}$
u_∞	=	freestream velocity magnitude
Δ	=	local Cartesian grid spacing
Δt_{samp}	=	probe-output sampling interval
λ	=	roll angle
σ	=	total angle of incidence

*Corresponding author.

σ_{C_l}	=	sample standard deviation of the C_l time series
τ_{int}	=	integral timescale of the C_l time series

Subscripts and abbreviations

∞	=	freestream condition
G_1, G_2, G_3	=	coarse, reference, and fine grids of the present mesh family
wing k	=	contribution integrated over surface of Wing k, $k \in \{1, 2, 3, 4\}$
CTU	=	convective time unit, CTU = d_{ref}/u_∞
LES	=	large eddy simulation
MUPS	=	million cell updates per second (solver throughput)
PSD	=	power spectral density
RANS	=	Reynolds-averaged Navier–Stokes
WMLES	=	wall-modeled large eddy simulation

I. Introduction

A research program has been underway under the NATO Science and Technology Organization (STO), Applied Vehicle Technology (AVT) panel to understand the prediction of vortex-dominated flows about generic missile airframes. The program has spanned two task groups, AVT-316 ("Vortex Interaction Effects Relevant to Military Air Vehicle Performance") and AVT-390 ("Vortex Flow Predictions for Stability and Control of Missile Airframes"). Initial contributions from AVT-316 were reported in Special Sessions at the AIAA SciTech meeting in January 2022 [1–4], and AVT-390 results were first presented in a Special Session at the AIAA AVIATION Forum 2024 [5–9]. The present paper contributes to the AVT-390 Special Session at AIAA AVIATION Forum 2026, and builds directly on a prior 2024 SciTech contribution by the present authors [10].

The central validation target of AVT-390 is a generic missile airframe developed by the German Aerospace Center (DLR), the LK6E2, whose transonic aerodynamics at moderate to high angles of incidence exhibits a break in rolling moment that has proven difficult to capture. The geometry is shown in Figure 1. At roll angle 45° and $M_\infty = 0.85$ the airframe develops an asymmetric vortex system between the windward and leeward wing pairs; as the angle of incidence σ is increased through the range covered by the wind-tunnel measurements, the lee-side vortex system reorganizes in a way that produces a step change in C_l. Experimentally, a primary break occurs near $\sigma \approx 16°$, and a weaker secondary break is observed in the neighborhood of $\sigma \approx 14°$; both features are pronounced only at $M_\infty = 0.85$, implicating shock-vortex interactions in their origin [7].

Diverse numerical approaches have been brought to bear on this case within the task group, including RANS sensitivity studies and compressibility-model comparisons [7, 11], anisotropic adaptive-mesh RANS [12], hybrid RANS–LES / DES using multiple solvers and modelling choices [8], and the WMLES results contributed previously by the present authors [10]. Together these efforts have produced a picture in which the primary break is by now well-characterized: around $\sigma \approx 15°$ the leading normal shock on Wing 4 diminishes, the flow separation topology on Wing 4 reorganizes, and a large region of separated flow develops on the outboard leading edge [7]. Different methods achieve this qualitative picture through different modelling routes, and quantitative agreement with the DLR HST and TWG wind-tunnel measurements [6] has improved as the task group has matured.

The contribution of the present paper is twofold. First, the angle-of-incidence sweep reported in [10] is extended downward to cover the $\sigma \approx 13°$ to 15° range that samples the weaker, secondary break in C_l. That earlier sweep did not cluster points in this regime; the new simulations presented here do. Second, power spectral densities of pressure are computed at a set of numerical probes that match those used in the scale-resolving simulations of Tormalm *et al.* [8]. The WMLES power spectral density (PSD) spectra show qualitative features that differ from the spectra reported by the other scale-resolving approaches in the task group; a dedicated section reports the observations and discusses possible physical explanations. The intent is to add one more observation to the collective picture that the task group is assembling, rather than to rank methods.

The paper is organized as follows. Section II briefly recaps the solver, case setup, and mesh family used for the new simulations. Section III reports a grid-refinement study at three angles spanning the regimes of interest. Section IV presents the extended angle sweep and the per-surface rolling-moment decomposition that makes the two-break structure visible. Section V reports the probe PSD spectra and the comparison with the reference results of [8].

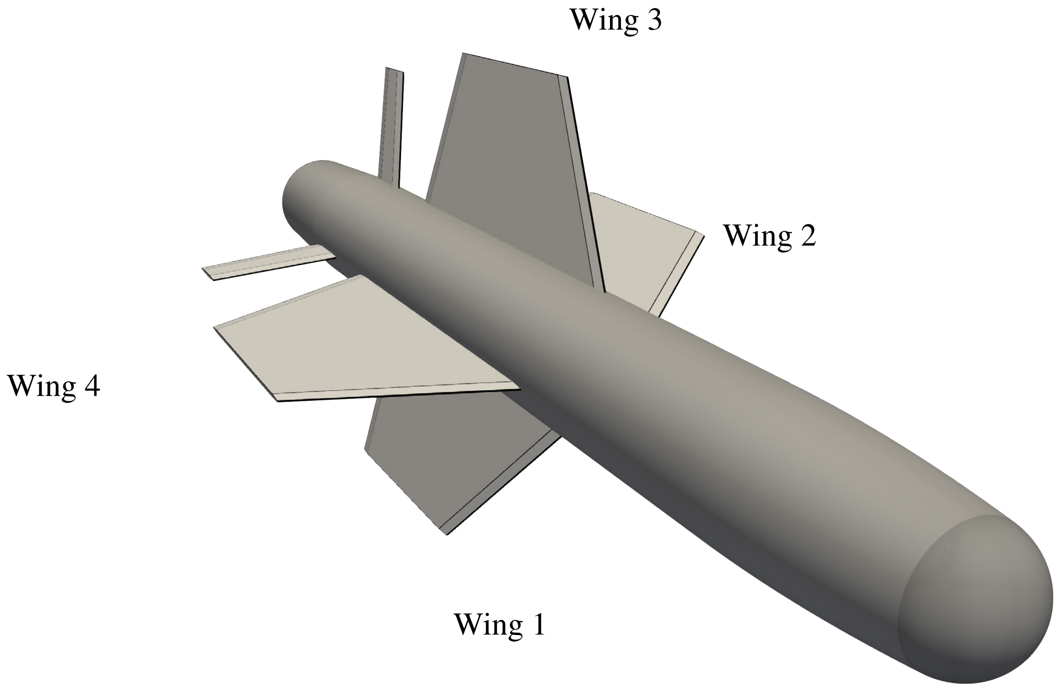

Fig. 1 The DLR LK6E2 airframe in the $\lambda = 45°$ rolled configuration. Surface is shaded by curvature to highlight edges.

II. Numerical Method and Case Setup

A. Volcano ScaLES

All simulations in the present work are carried out with Volcano ScaLES, a GPU-native, Cartesian-octree, compressible Navier–Stokes solver targeted at wall-modeled large eddy simulation (WMLES) of configurations with industrially-relevant geometry. The solver is written in C++17 and CUDA, uses a nominally fourth-order finite-difference discretization of the convective fluxes with favorable kinetic-energy and entropy-consistency properties, a blend of fourth- and second-order stencils for the viscous fluxes tailored to high-Reynolds-number turbulence, a dynamic Smagorinsky sub-grid model [13, 14], and the third-order Strong-Stability-Preserving Runge–Kutta time integrator of Shu and Osher [15–17]. Geometries are represented using an immersed-boundary method with an algebraic equilibrium wall model that applies a shear-stress constraint using flow information sampled at a fixed off-wall distance of $3\Delta/2$, where Δ is the local grid spacing. A shock-capturing scheme driven by physics-based discontinuity sensors is activated when needed; the associated numerical dissipation is highly localized in the regions flagged by those sensors. A complete description of the solver, together with its application to the present test case, is provided in [10]; the discussion here is limited to what is necessary to follow the rest of the paper. ScaLES has also been validated on a wide variety of CFD applications [18–25].

The solver is explicit in time and requires on the order of 100 megabytes of GPU memory per million cells, which enables billion-cell-scale LES on a small number of commodity GPUs. The simulations reported in Section IV were run on workstation-class GPU nodes equipped with eight NVIDIA RTX PRO 6000 Blackwell Server Edition cards (96 GB/card) or eight NVIDIA L40S cards (48 GB/card); representative throughput on both configurations is reported in Table 4.

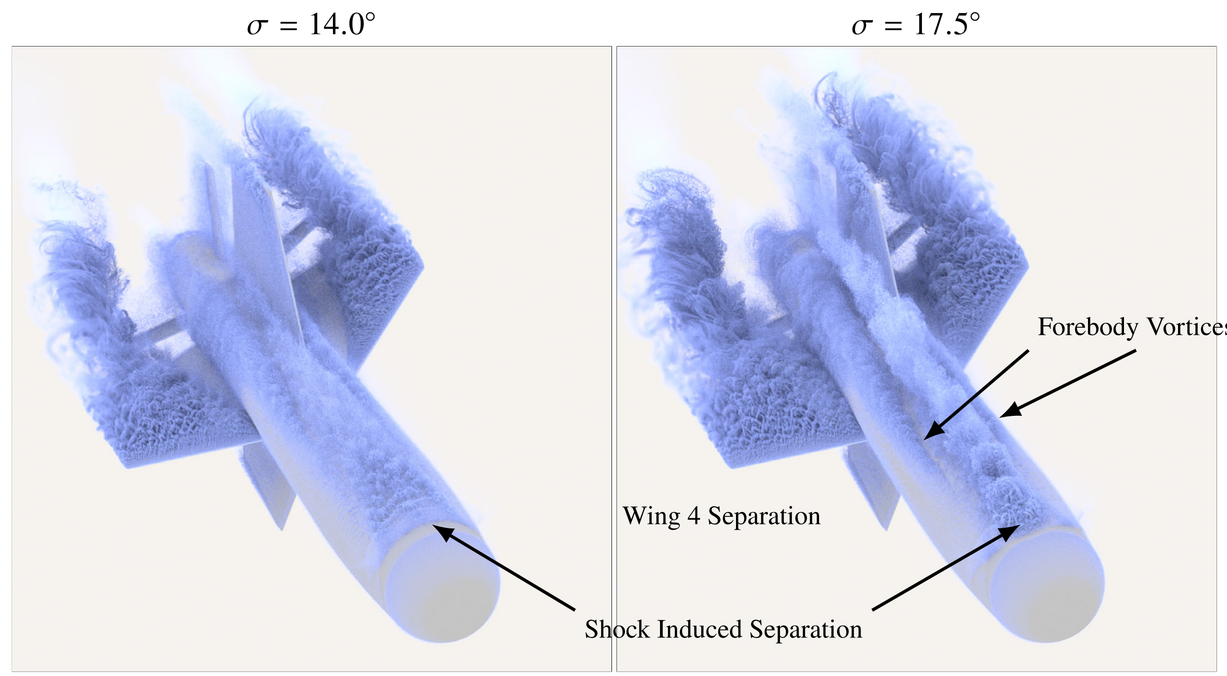

Fig. 2 Comparison of turbulent flow features for angle of incidence $\sigma = 14°$ and $\sigma = 17.5°$. As the angle increases, the forebody vortices and nose separation become more prominent and there is a loss of coherent vortical flow over the wings.

B. Geometry and Flow Conditions

The geometry is the DLR LK6E2 generic missile airframe in the canonical $\lambda = 45°$ rolled configuration, matching the DLR HST and TWG wind-tunnel campaigns [6]. Simulations are carried out in free air on a domain of side $200d_{\text{ref}}$, where $d_{\text{ref}} = 0.05$ m is the reference body diameter, centered on the missile. Flow conditions are identical to those of [10] and are summarized in Table 2. The total angle of incidence σ is the only quantity varied across the campaign; it enters through the initial velocity vector, which, together with the Mach number and speed of sound defined by Table 2, sets the initial freestream. All runs are initialized from uniform freestream.

Table 2 Nominal freestream and reference conditions, shared across the full sweep. Conditions match the DLR HST/TWG test envelope at $M_\infty = 0.85$. The convective time unit CTU = d_{ref}/u_∞ derived from these conditions (with $u_\infty \approx 280$ m s^{-1} at $M_\infty = 0.85$ and the listed T_∞) is 1 CTU ≈ 179 μs; nondimensional times are reported as $t^\star = t/\text{CTU}$.

Static pressure p_∞ [Pa]	Static temperature T_∞ [K]	Roll angle λ [deg]	Mach number M_∞ [–]	Ref. length d_{ref} [m]
47 075	270	45	0.85	0.05

C. Mesh

The Cartesian-octree mesh topology used for the present simulations is unchanged from [10], i.e. the same refinement regions are used. It is worth noting that the meshing procedure is not exactly the same; the new meshes conform more closely to the body resulting in slightly fewer grid points for a given spacing. Figure 3 shows a cross-section view of the mesh refinement topology. The mesh design is achieved simply with two nested conical volume refinement regions and some additional refinement above Wing 2 and Wing 4. A zoomed in view of all three meshes over the leading edge of Wing 2 is shown in Figure 4. Three uniform-h refinements of that topology are employed, labelled G_1, G_2, and G_3 in order of increasing resolution and summarized in Table 3. The G_2 grid is the reference grid used for the main angle-of-incidence sweep of Section IV; G_1 and G_3 serve as the bracketing resolutions for the grid-refinement study of Section III.

Table 3 Parameters of the mesh family used in the present campaign. The spacing *h* is the finest Cartesian cell size; cell counts are reported in millions.

Label	h [mm]	Cells [10^6]	Role
G_1	6.87×10^{-2}	675	coarse-bracket
G_2	6.14×10^{-2}	917	reference sweep grid
G_3	5.49×10^{-2}	1257	fine-bracket

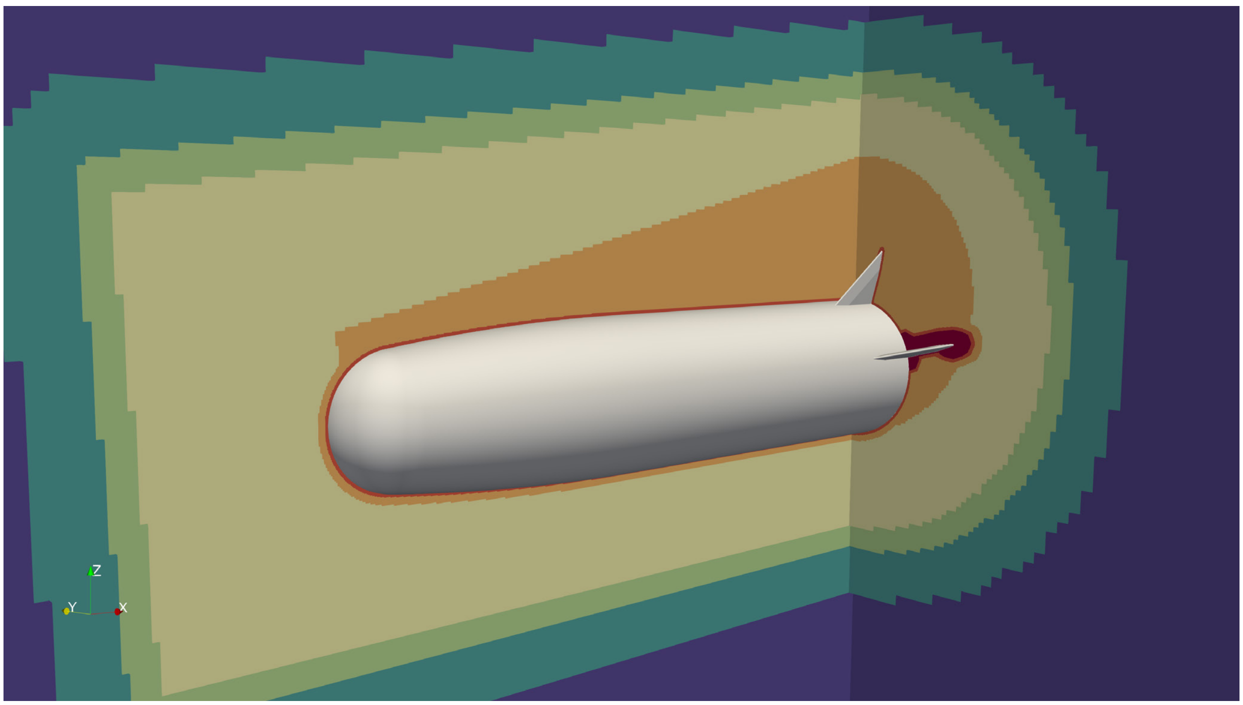

Fig. 3 Constant *y*- and *x*-slices showing the refinement topology used in this work. There are two volume refinement cones (yellow and orange) to capture off-body vorticity and large refinement regions above Wing 2 and Wing 4 for the leading edge vortex (dark red).

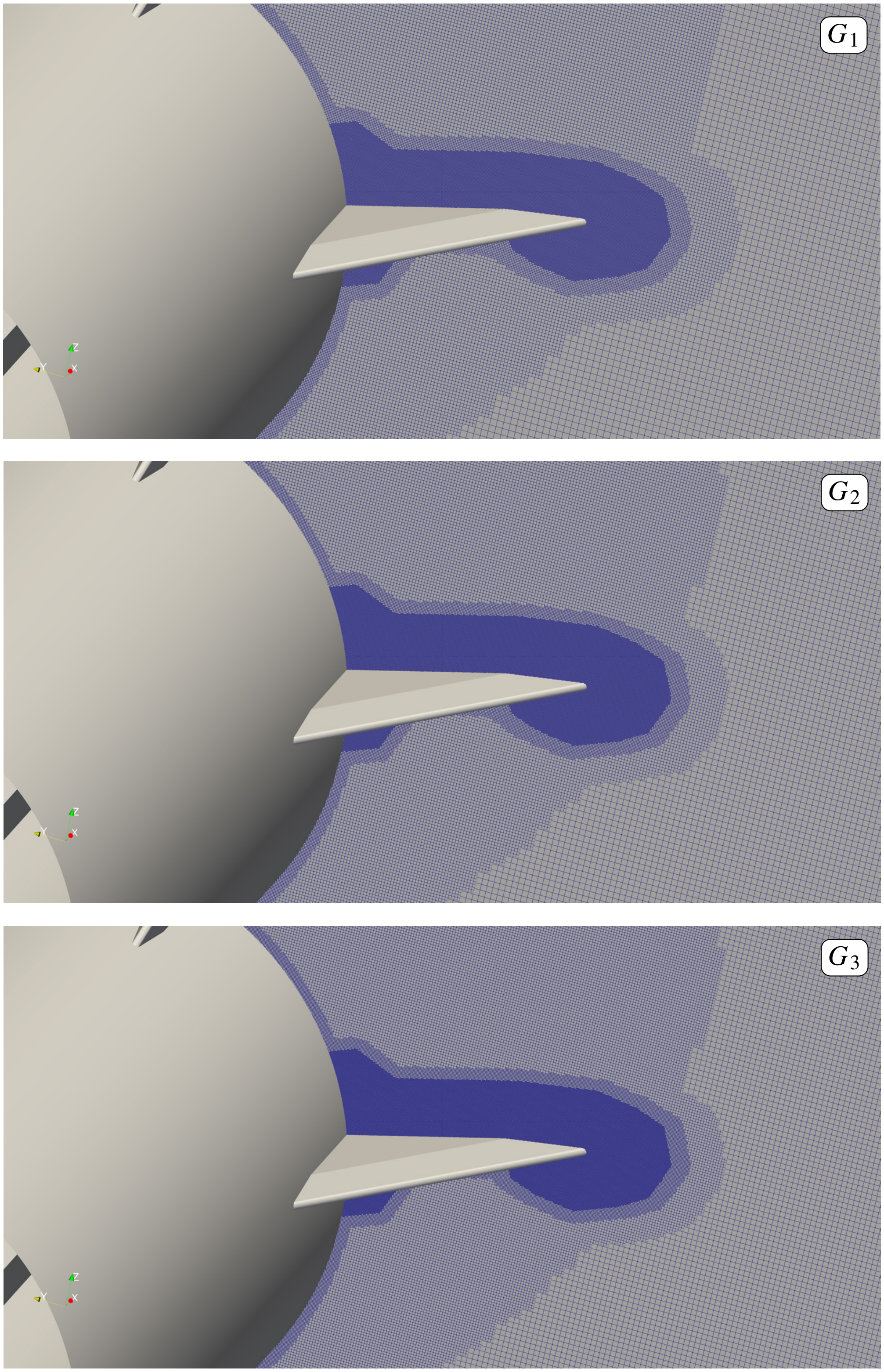

Fig. 4 Constant $x = -0.22$ m slice of the computational mesh looking downstream over the leading-edge of Wing 2.

D. Simulation Campaign

The present study covers the angle-of-incidence range $\sigma \in [13°, 19°]$, sampled at ten points chosen to resolve both the primary break near $\sigma \approx 16°$ and the secondary break near $\sigma \approx 14°$, with denser clustering across the secondary-break region. All runs in the angle-of-incidence sweep use the G_2 grid; the bracketing G_1 and G_3 grids are exercised in the grid-refinement study of Section III. Representative solver throughput on the two GPU node configurations used for the campaign is reported in Table 4.

Table 4 Representative Volcano ScaLES throughput on the G_2 grid (917 million cells), 8 GPUs per node, for the two node configurations used in the present campaign. MUPS is mega cell updates per second.

GPU node	GPU memory	MUPS	Wall time / CTU
8× NVIDIA RTX PRO 6000 Blackwell	96 GB/card	≈ 10 500	7.2 min
8× NVIDIA L40S	48 GB/card	≈ 6 650	11.3 min

III. Grid Refinement Study

To establish the grid sensitivity of the integrated rolling moment that is reported in Section IV, three angles are simulated on each of the three grids of Table 3: $\sigma = 14°$, sampling the secondary-break regime; $\sigma = 16°$, sampling the primary break; and $\sigma = 17.5°$, sampling the post-primary-break regime.

Figure 5 reports $\overline{C_l}$ on each grid at each angle, with vertical bars indicating the integral-timescale-corrected uncertainty in the mean [26]. The behavior is regime-dependent. At $\sigma = 14°$, refinement from G_1 to G_3 is monotonic: $\overline{C_l}$ moves continuously toward more negative values as h is reduced. At $\sigma = 16°$, the trend is non-monotonic in h and the total G_1–G_3 spread is approximately 4% of the G_2 mean. At $\sigma = 17.5°$, G_1, G_2, and G_3 agree to within their uncertainty and are statistically indistinguishable. Two points are worth highlighting:

1) The lack of monotonic convergence at $\sigma = 16°$ indicates G_2 is not in the asymptotic-convergence regime in a rigorous sense, however the spread is comparable in magnitude to the spread of the experimental envelope at the same σ.
2) None of the grids failed to produce the rolling-moment break, even the coarsest mesh G_1. This suggests that any of the resolutions is sufficient to capture the correct physical phenomena for the *primary* break near $\sigma = 16°$. There does appear to be an advantage to using G_2 at $\sigma = 14°$ near the much weaker *secondary* break.

Based on these observations, G_2 is used to complete the remaining sweep angles based on its improved accuracy for lower values of σ.

IV. Angle-of-Incidence Sweep

A. Experimental Reference Data

The DLR HST/TWG wind-tunnel campaign on the LK6E2 provides four reference data sets at $M_\infty = 0.85$: two roll configurations (nominal $\lambda = \pm 45°$) measured in each of the two tunnels [6]. Because the airframe is symmetric about the $\lambda = 0$ plane, measurements at roll +45° and roll −45° describe the same physical configuration with the rolling-moment sign reversed; after a uniform sign convention is imposed, the four data sets are combined into a single envelope whose span at each σ is the spread between facilities and roll configurations. All rolling-moment plots below are reported in the wind-tunnel convention: positive C_l corresponds to positive roll from Wing 4 toward Wing 2.

B. Integrated Forces and Moments

Figure 6 shows the mean rolling moment C_l from the present campaign plotted against the angle of incidence σ, with the combined HST/TWG envelope overlaid. The simulation means are drawn as unfilled markers connected by a dashed line; vertical bars indicate the estimated uncertainty of the mean. Quantitative agreement with the wind-tunnel envelope is good across the full sampled range $13° \leq \sigma \leq 19°$, including the lower-σ portion which was not addressed in [10]. The primary break in C_l near $\sigma \approx 16°$ is recovered to the same fidelity reported previously; the secondary break near $\sigma \approx 14°$ is captured as well, and is the main new result.

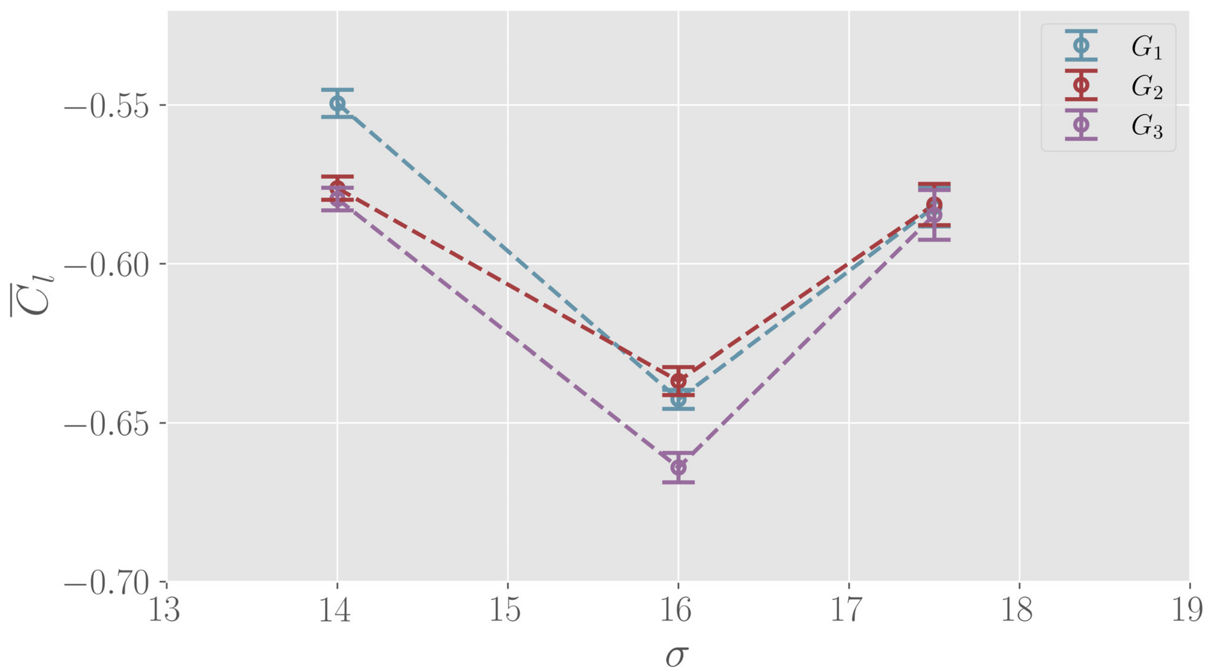

Fig. 5 Grid-refinement study at σ = 14°, 16°, and 17.5° on G_1, G_2, and G_3. Open circles: mean C_l over the statistically stationary window; vertical bars: mean error estimates.

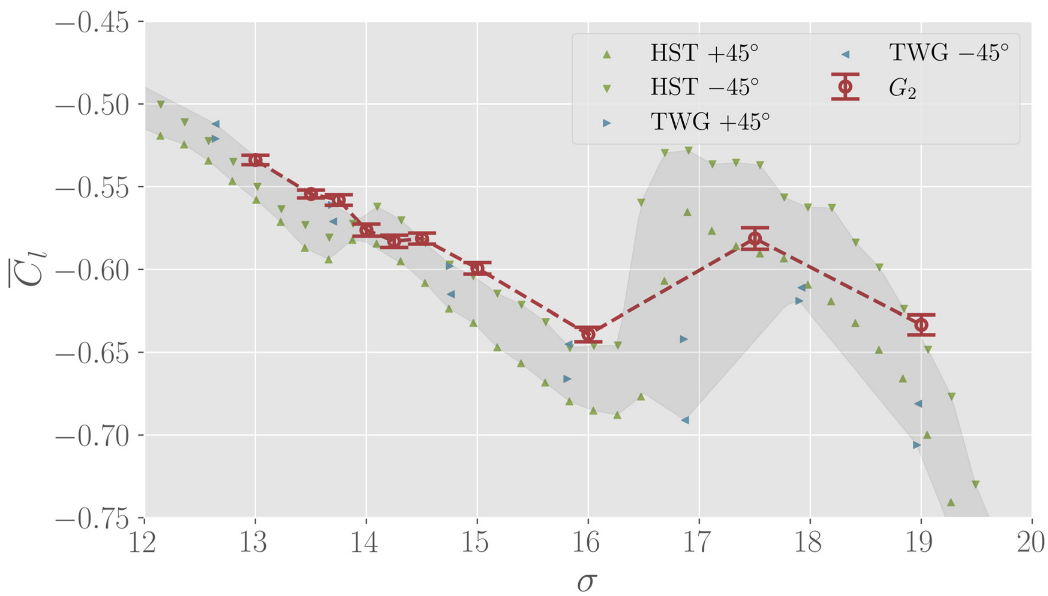

Fig. 6 Mean rolling moment $\overline{C}_l$ versus angle of incidence σ on the G_2 grid. Open circles with vertical bars: means with estimated uncertainty; dashed line connects the means as a guide to the eye. The shaded gray band is the envelope of the four DLR wind-tunnel records (HST and TWG facilities, both rolls) at M_∞ = 0.85 [6]; the individual records are shown as markers within the band.

Load histories for all ten angles are collected in Figure 7. Each panel shows the instantaneous C_l trace, the mean computed over the statistically stationary portion of the record (dashed line), and the one-standard-deviation fluctuation envelope (shaded band). The shaded gray bands indicate the local experimental spread at that σ. The histories in the lower-σ regime show substantially smaller fluctuation levels than at higher σ, consistent with the progressive loss of coherent leading-edge vortex dynamics over Wing 4 discussed in Section IV.C.

C. The Two Breaks in the Rolling-Moment Curve

The wind-tunnel $C_l(\sigma)$ curve exhibits two distinct features: a primary break in the neighborhood of $\sigma \approx 16°$ and a secondary, weaker break in the neighborhood of $\sigma \approx 14°$. Both are observed only at $M_\infty = 0.85$ in the $0.3 \leq M_\infty \leq 0.85$ measurement range reported in [7]; the identification of a Mach-number threshold makes it clear that shocks play a causal role in both features.

The primary break. The mechanism for the primary break has been characterized by Anderson *et al.* [7] on the basis of RANS solutions and is consistent with the present WMLES results. As σ is increased through approximately 15°, the leading normal shock on Wing 4 diminishes and eventually vanishes; the separation topology on Wing 4 reorganizes, producing a large region of separated flow on the outboard section of the leading edge and breaking down the leading-edge vortex. Figure 8 shows constant-y slices of Mach number for Wing 2 and Wing 4 at $\sigma = 16°$, 17.5°, and 19°. At $\sigma = 16°$ the adverse pressure gradient near the leading edge of Wing 4 has already reduced to a smoother gradient although the shock is not fully gone; beyond 16° the pressure gradients over Wing 4 collapse, massive flow separation occurs, and a weaker normal shock settles connecting Wing 4 and Wing 3. Throughout this range the shock structure on Wing 2 remains comparatively stable: the roll angle causes the incoming flow to approach Wing 2 glancingly while Wing 4 tilts more into the freestream and sees higher incoming momentum.

The secondary break. The new angles $\sigma \in \{13°, 13.5°, 13.75°, 14°, 14.25°, 14.5°, 15°\}$ sample the secondary-break regime directly, with denser clustering across 13.75°–14.5° where the wind-tunnel data show the kink in $C_l(\sigma)$. Figure 9 plots constant-y Mach number slices over Wings 2 and 4 at $\sigma = 13°$, 14°, 15° as representative samples of the regime. At $\sigma = 13°$ two normal shocks are visible on Wing 4; the adverse pressure gradient from the leading shock diverts the separated flow inboard from the leading edge. At $\sigma = 14°$ the leading shock is weaker and fluctuations behind it suggest rotational flow beginning to pass across it, but the separated flow is still largely confined to the leading edge. By $\sigma = 15°$ the leading normal shock on Wing 4 is nearly diminished and the outboard separated region has begun to spread. On the Wing 2 side the leading shock weakens more gradually and remains present throughout. The denser samples at $\sigma = 13.5°$, 13.75°, 14.25°, and 14.5° fall continuously between these representative cases, without discrete reorganization events between adjacent angles.

These observations support a view of the secondary break as an *incipient* form of the primary-break reorganization: the same Wing 4 leading-shock weakening and outboard-separation spread that drive the primary break are already under way at $\sigma \approx 14°$, but have not yet propagated far enough to collapse the leading-edge vortex system. In the integrated rolling moment, the kink localizes to $\sigma \in [14.25°, 14.5°]$ in the present WMLES: the slope $\mathrm{d}C_l/\mathrm{d}\sigma$ flattens between these two angles, before resuming its mean trend toward the primary break.

A view of the full-wing pressure pattern complements the slice and footprint visualizations above. Figure 10 shows the mean surface pressure coefficient $\overline{C}_p$ at three angles spanning the sweep: $\sigma = 14°$ (pre-both-breaks), 16° (just past the secondary break, approaching the primary break), and 17.5° (past the primary break). The progression captures the surface-pressure signature of the mechanisms described above. At $\sigma = 14°$ the leading-edge suction is moderate and the pressure pattern on both windward wings (Wings 2 and 4) is broadly symmetric. By $\sigma = 16°$ the suction footprint on Wing 4 has deepened and extended toward the trailing edge, consistent with the weakening leading shock and the beginning of outboard-separation spread; the Wing 2 footprint evolves more gradually, consistent with the glancing-flow interpretation in Section IV.C. By $\sigma = 17.5°$ the Wing 4 leading-edge suction region has broadened into a large low-$\overline{C}_p$ zone spanning most of the surface, with a visible recompression line across mid-chord that marks the foot of the weaker trailing shock predicted by Figure 8. In the same figure, the experimentally measured pressure coefficient is shown in the right column.

D. Per-Surface Decomposition

A feature of the LK6E2 configuration at $\lambda = 45°$ is that the net rolling moment is a near-cancellation of the contributions from Wings 2 and 4. At $\sigma = 16°$, for example, the per-wing contributions are of order $|C_{l,\mathrm{wing}}| \approx 4$ while the net is of order $|C_l| \approx 0.6$—a residual of ~15% of either contribution. Figure 11 plots this decomposition. The top

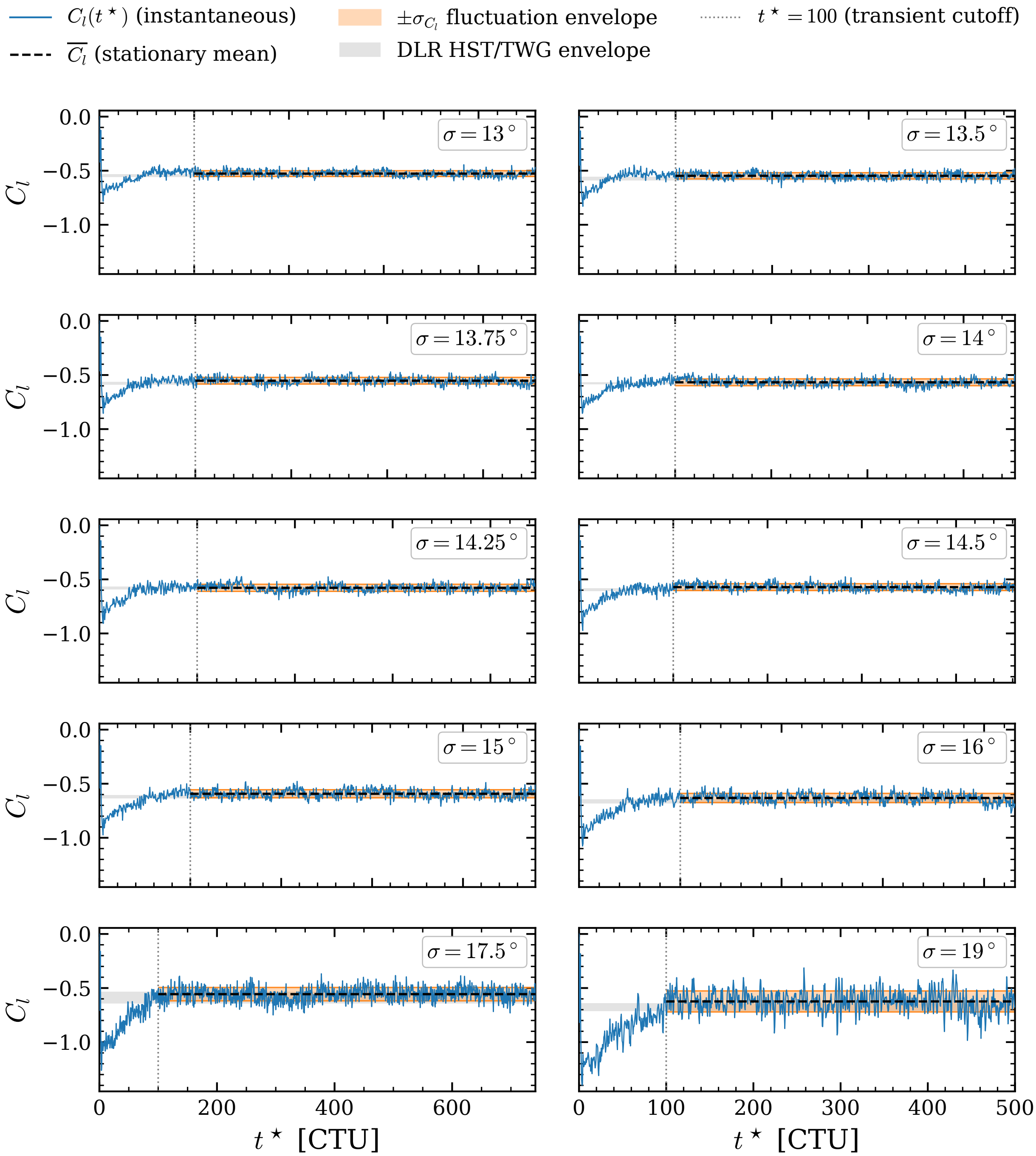

Fig. 7 Instantaneous rolling-moment histories for each angle of the sweep on the G_2 grid, in left-to-right top-to-bottom order of increasing σ. Blue trace: instantaneous $C_l(t^\star)$; dashed line: mean over the statistically stationary window ($t^\star > 100$ CTU); shaded orange: $\pm\sigma_{C_l}$ fluctuation envelope around that mean (the standard deviation σ_{C_l} is distinct from the angle of incidence σ); shaded gray: experimental spread of the DLR HST/TWG envelope at the corresponding angle. The vertical dotted line marks the start of the statistically stationary window.

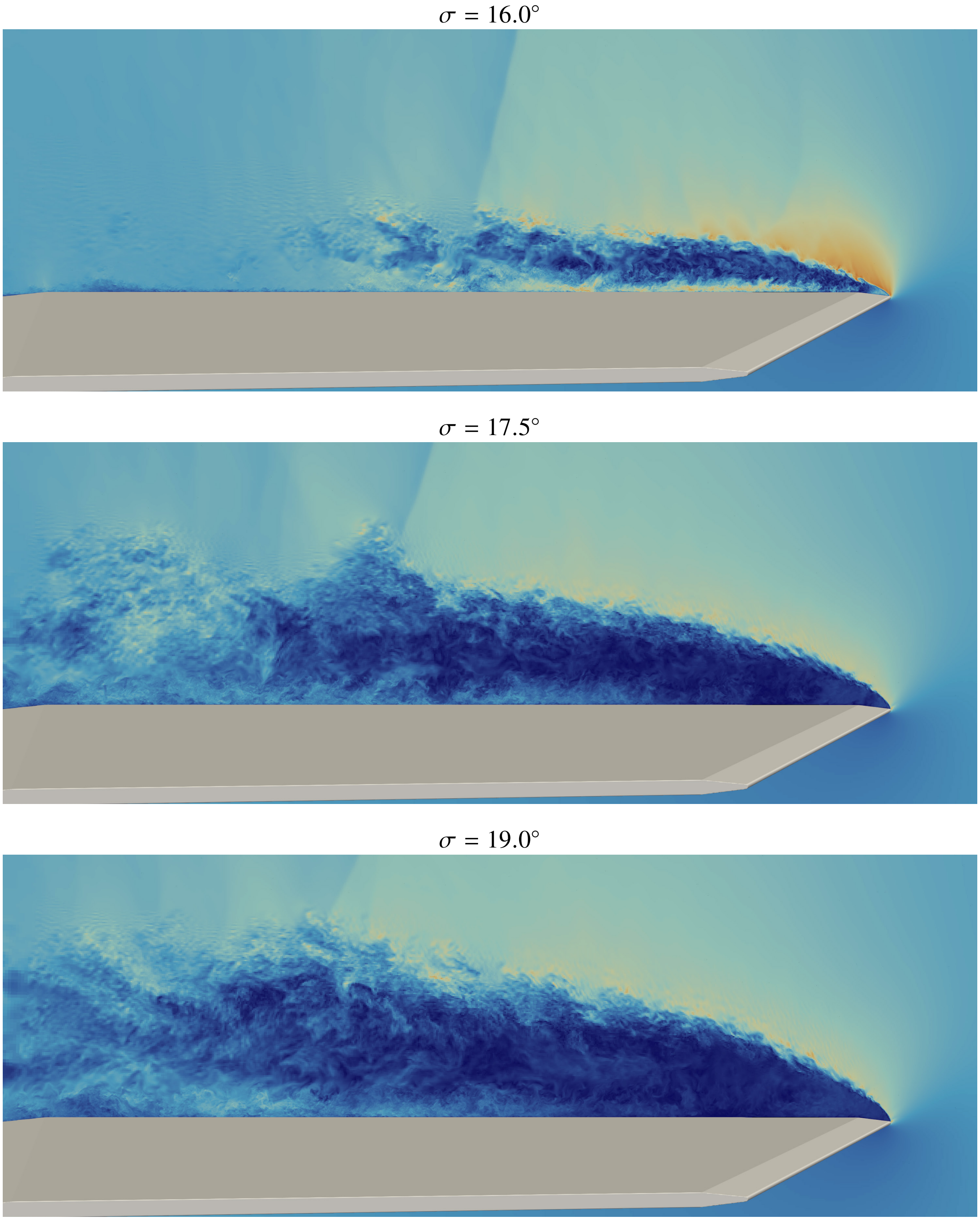

Fig. 8 Constant-y slices of Mach number over Wing 4 on the G_2 grid for σ = 16°, 17.5°, and 19° (top to bottom), illustrating the primary-break mechanism.

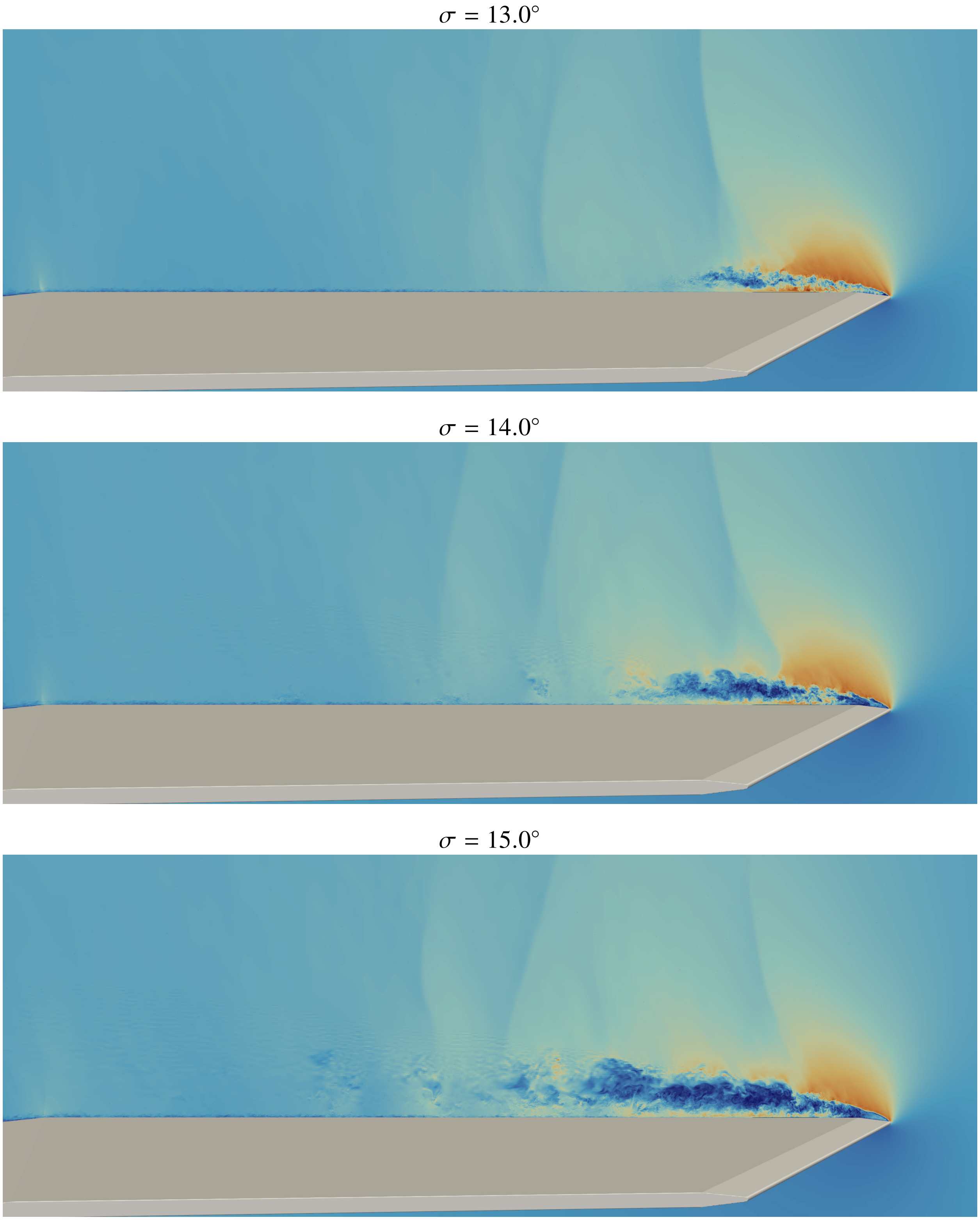

Fig. 9 Constant-y slices of Mach number over Wing 4 on the G_2 grid for σ = 13°, 14°, and 15° (top to bottom), illustrating the secondary-break mechanism. The leading normal shock on Wing 4 weakens progressively through this range; the shock structure on Wing 2 (not shown) stays comparatively stable over the same range.

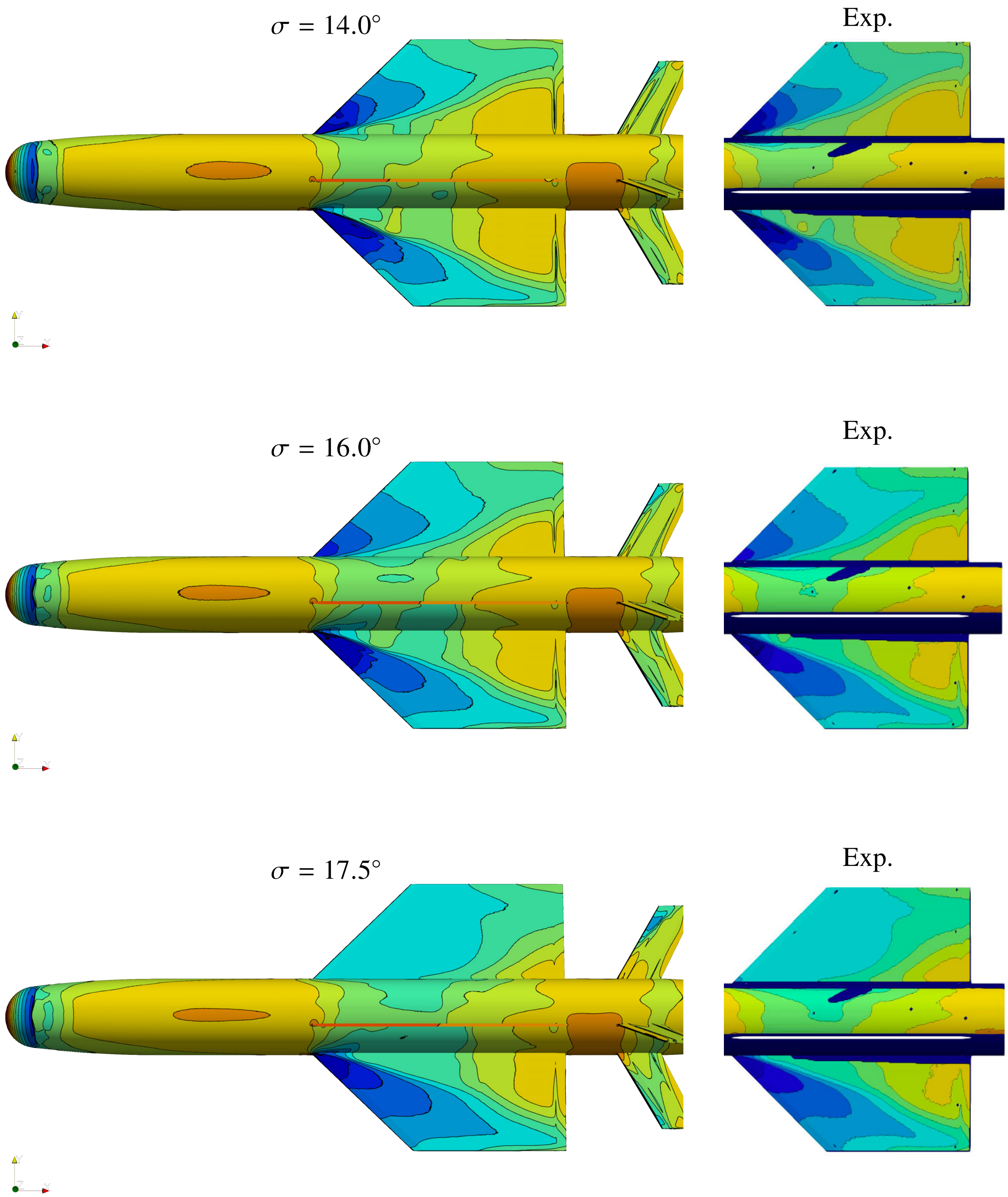

Fig. 10 Mean surface pressure coefficient $\overline{C}_p$ over the missile body and wings at σ = 14°, 16°, 17.5° (top to bottom), viewed from above with the freestream entering from the left. Nose stagnation, leading-edge suction, and shock signatures evolve across the sweep consistently with the mechanisms described in the text. Experimental data for the wings are shown in the right column.

panel shows the C_l contribution for each wing. The bottom panel reports the slope $\mathrm{d}\overline{C_l}/\mathrm{d}\sigma$ for each wing, computed by centred difference which indicates the portions of the sweep in which each wing's loading rate changes character.

The slope panel attributes the secondary break to Wing 4. Across the lower-σ arm, $\mathrm{d}\overline{C_{l,\mathrm{wing2}}}/\mathrm{d}\sigma$ remains essentially constant, while $\mathrm{d}\overline{C_{l,\mathrm{wing4}}}/\mathrm{d}\sigma$ changes abruptly between $\sigma = 13.5°$ and $14.5°$. The slope contributions from Wings 1 and 3 are an order of magnitude smaller and are flat through the same interval. The total C_l slope flattening reported in Section IV.C therefore reflects almost entirely a softening of the Wing 4 loading rate, in the same σ range over which Figure 9 shows the Wing 4 leading shock weakening.

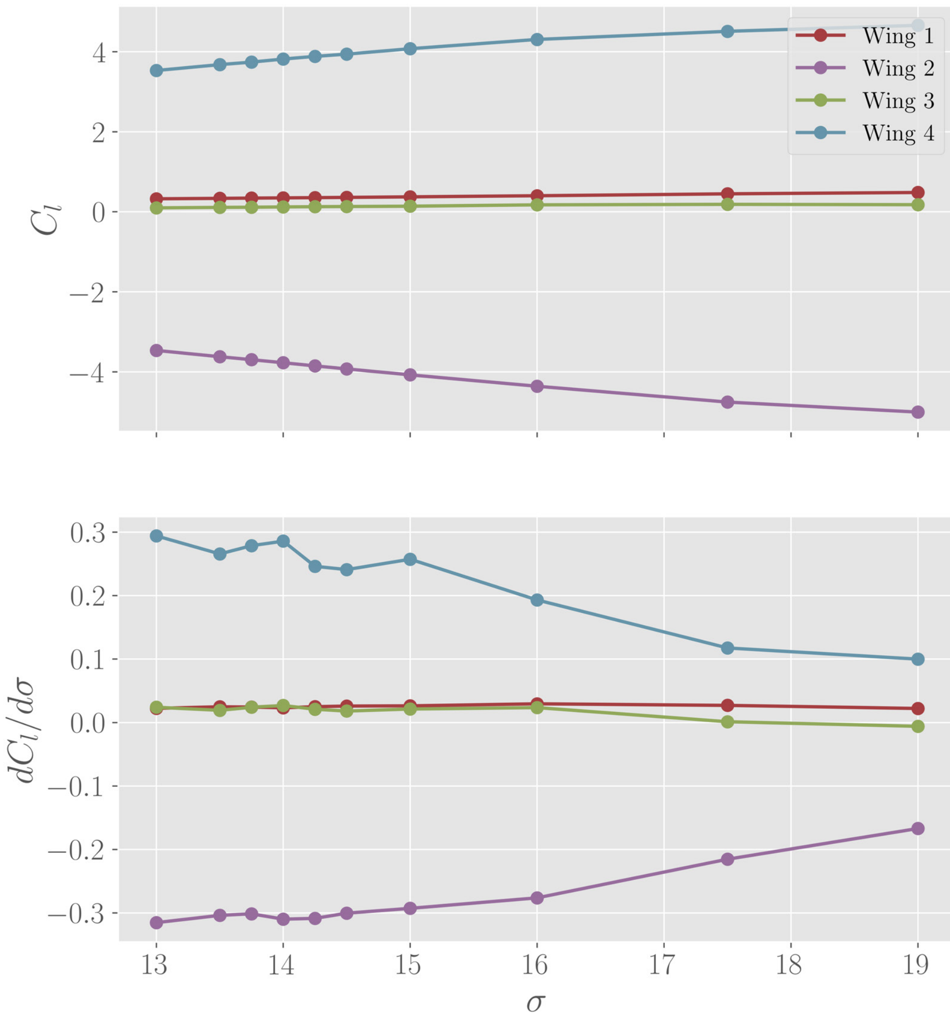

Fig. 11 Top: per-wing decomposition of the rolling moment $\overline{C_l}$ versus angle of incidence on the G_2 grid. Bottom: $\mathrm{d}\overline{C_l}/\mathrm{d}\sigma$ for each wing.

V. Power Spectral Density at Numerical Probes

Tormalm *et al.* [8] report probe pressure power spectral density (PSD) spectra from scale-resolving simulations at $\sigma = 17.5°$, $\lambda = 45°$, $M_\infty = 0.85$ and identify a dominant peak near 1–1.1 kHz across most of the instrumented probes, with additional higher-frequency content near the nose consistent with forebody-vortex shedding. They interpret the observed Strouhal numbers as close to those of cylindrical-wake shedding and attribute the dominant content to the shedding from the missile forebody and its downstream impingement on Wing 3. They also note that "further analysis of frequency content is needed," and defer a more complete treatment to the eventual NATO STO report.

This section reports probe PSDs from the present WMLES at the same operating point and at the same sixteen probe locations, so the comparison with [8] is direct. The outcome is qualitatively different from the hybrid RANS–LES results in several respects, discussed in Section V.C.

A. Probe Set and Signal Processing

The probe layout used in the present simulations is a superset of the sixteen locations P1–P16 defined in Table 3 of [8]. The subset matching those locations is retained for the comparison reported below; the remaining probes sample supplementary locations that are not discussed here. Unsteady pressure is sampled at a fixed probe-output cadence, $\Delta t_{\mathrm{samp}} = 1.79\ \mu$s, yielding a sampling rate $f_s = 560$ kHz and a Nyquist limit $f_{\mathrm{Nyq}} = 280$ kHz. This cadence is two orders of magnitude above the ~ 1 kHz scale reported as dominant in [8], so no aliasing is anticipated in the band of physical interest.

Table 5 Sampling for the probe data used in the present PSD analysis using Welch's method. N_{samples} is the number of samples retained after transient trimming; $T^\star$ is the corresponding record span in convective time units $t^\star = t\,u_\infty/d_{\mathrm{ref}}$; Δt_{samp} is the probe-output interval; N_{seg} is the number of segments each containing 2048 snapshots with 50% overlap; $\Delta f = 1/(N_{\mathrm{seg}}\,\Delta t_{\mathrm{samp}})$ is the resulting frequency resolution.

Record	N_{samples}	$T^\star$	Δt_{samp} [μs]	f_{Nyq} [kHz]	N_{seg}
17.5	42 480	425	1.79	280	40

Each probe pressure record is processed as follows: because the solver time step is adaptive, the raw probe record is first resampled onto a uniform time grid of the same length via piecewise-linear interpolation; this yields a uniform sample spacing Δt_{samp} equal to the mean probe-output interval over the stationary window. The sample mean is subtracted, the leading transient is trimmed, and the remainder is split into overlapping segments of length $N_{\mathrm{seg}} = 2048$ with 50% overlap. A Hamming window is applied to each segment, and Welch's method [27] is used to estimate the power spectral density. At $\Delta t_{\mathrm{samp}} = 1.79\ \mu$s this yields $\Delta f \approx 273$ Hz, adequate to resolve the ~ 1 kHz peak reported in [8]. Spectra are reported in physical units (frequency in Hz, PSD amplitude in Pa^2/Hz) so that amplitude-level comparisons with the spectra in [8] are direct modulo the windowing and segmentation differences discussed in Section V.C. For orientation, the ~ 1 kHz peak in [8] corresponds to Strouhal number $\mathrm{St} = f d_{\mathrm{ref}}/u_\infty \approx 0.18$ (using $d_{\mathrm{ref}} = 0.05$ m and $u_\infty = 280\ \mathrm{m\,s^{-1}}$), and the nose-probe ~ 4 kHz feature to $\mathrm{St} \approx 0.77$.

B. Results

Figure 13 collects the pressure PSD spectra at the four probes P2, P4, P7, and P10. The locations of these probes are shown in Figure 12. These four locations span the principal flow regions relevant to the comparison with [8]: the Wing 3 apex / body junction (P2), the Wing 2 vortex / separated region at the mid-body (P4), the Wing 4 vortex / separated region (P7), and the Wing 3 side probe near the shock structure (P10).

The four probes show qualitatively different dominant frequencies. At P2 (Wing 3 / body junction) the dominant peak sits near 2 kHz with an amplitude of order 10^2 Pa^2/Hz, in the same frequency band as the peak reported in [8] for the corresponding probes. At P7 (Wing 4 leading-edge separated region) the dominant peak sits lower, near 0.5 kHz, with a broader skirt than a narrowband shedding tone would produce. At P4 (Wing 2 vortex / separated region) and P10 (Wing 3 side, near the shock structure), the dominant peak is at 0.4 kHz and 2.9 kHz respectively, but the bulk of the spectral energy in both probes lies in a substantially higher band (5–20 kHz at P4, with band-integrated power exceeding the 0.5–5 kHz band; 5–20 kHz at P10, comparable in band-integrated power to the 0.5–5 kHz band). Above the dominant peak, P2 displays a power-law decay with a slope of approximately $f^{-7/3}$ over the 2–20 kHz band, consistent with the Kolmogorov prediction for the pressure spectrum in locally isotropic turbulence [28]; the other three probes show shallower decays (between f^{-1} and $f^{-1.5}$ over the same band) consistent with shock-induced unsteadiness or wall-bounded scaling overlaying the Kolmogorov contribution.

C. Comparison with Other Scale-Resolving Simulations

The present WMLES probe spectra are compared with the hybrid RANS–LES results of Tormalm *et al.* [8] at $\sigma = 17.5^\circ$ and at the same sixteen probe locations. The raw probe pressure traces from five AVT-390 submissions have been processed through the same Welch's method used for the WMLES probes. Three categories of difference emerge. Figure 13 overlays the WMLES and other scale-resolving spectra at the four probes used throughout this section.

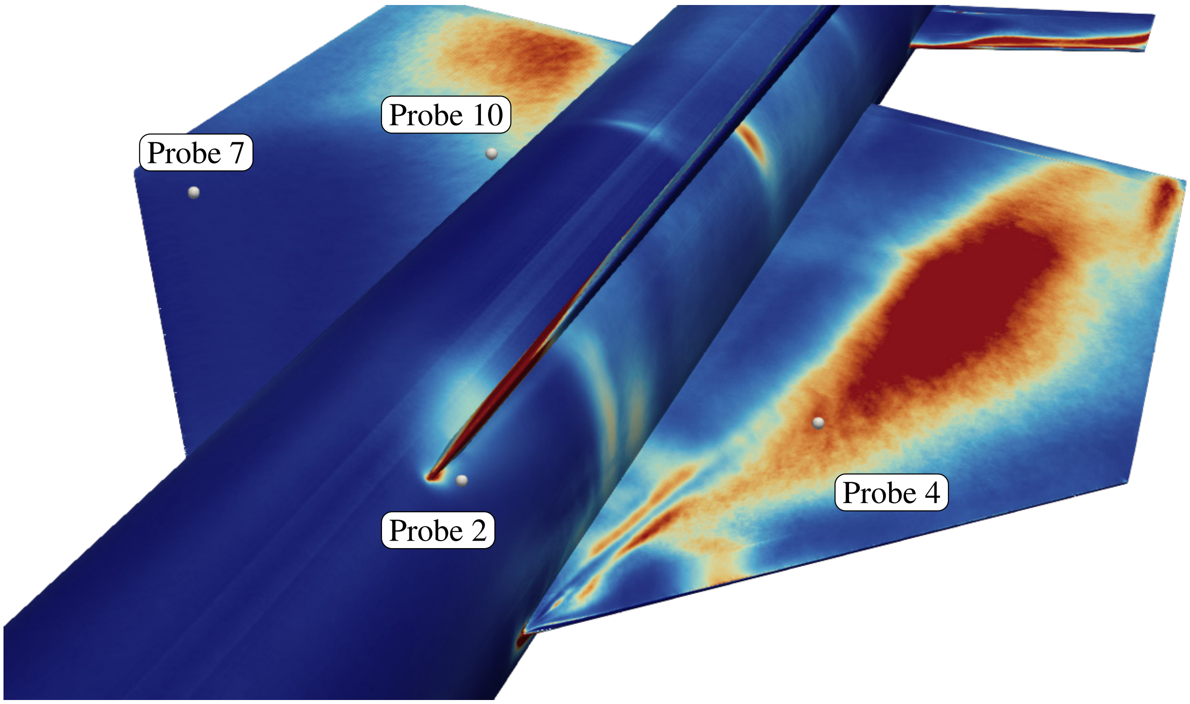

Fig. 12 Spatial locations of the four probes considered in this section for comparisons. Surface is shown colored by C_p variance for σ = 17.5°.

Breadth of the dominant peak. At P2 the FOI submissions cluster on a narrowband peak in the 1 kHz band with peak spectrum amplitudes of 10^3–10^4 Pa^2/Hz. The WMLES dominant peak at the same probe sits slightly higher in frequency (near 2 kHz) and at a peak amplitude near 10^2 Pa^2/Hz; the WMLES energy is correspondingly distributed over a broader frequency band rather than concentrated in a single peak. This difference is consistent with the two closure philosophies: the WMLES resolves a wider range of wall-bounded turbulence scales than the IDDES and HYB0 treatments used in [8], so coherent large-scale shedding coexists in the same spectrum with a broadband turbulent background whose energy fills in around the peak. Integrated band powers in the 0.5–5 kHz band are within a factor of a few across all six datasets at P2, indicating that the total energy carried by the dominant-peak band is comparable; the difference is in how that energy is distributed.

Background spectral slope. At P2 the WMLES decay slope above the peak is approximately $f^{-7/3}$ over the 2–20 kHz band, in the Kolmogorov-scaling for the pressure spectrum in locally isotropic turbulence [28]. The other scale-resolving submissions at the same probe show steeper decays over the same band, consistent with the hybrid models damping out scales above the resolved-modeled crossover. At the other separated-flow probes (P4, P7, P10) the WMLES decays are shallower than the Kolmogorov prediction, suggesting that shock-induced unsteadiness and wall-bounded scalings dominate the inertial-range contribution there. The near-Kolmogorov slope at P2, where the local flow is the cleanest candidate for an isotropic-turbulence interpretation, is an encouraging quantitative match.

Probe-to-probe consistency. The HYB0 submission shows a 1 kHz dominant peak at P4 and P10, this is consistent with the picture in [8] of a single forebody-shedding peak. The WMLES dominant peak frequencies are probe-dependent: ~ 2 kHz at P2, ~ 0.5 kHz at P7, ~ 0.4 kHz at P4, ~ 2.9 kHz at P10. The bulk of the spectral energy at P4 and P10 is carried in higher bands (5–20 kHz) rather than at the dominant peak. A probe-dependent peak frequency is consistent with multiple distinct unsteady mechanisms contributing at different stations. For example, forebody shedding at wing-junction probes, locally generated wall-bounded turbulence at vortex-core probes, and shock-foot unsteadiness at the side-shock probe. Disentangling these mechanisms requires a probe-by-probe examination against the corresponding

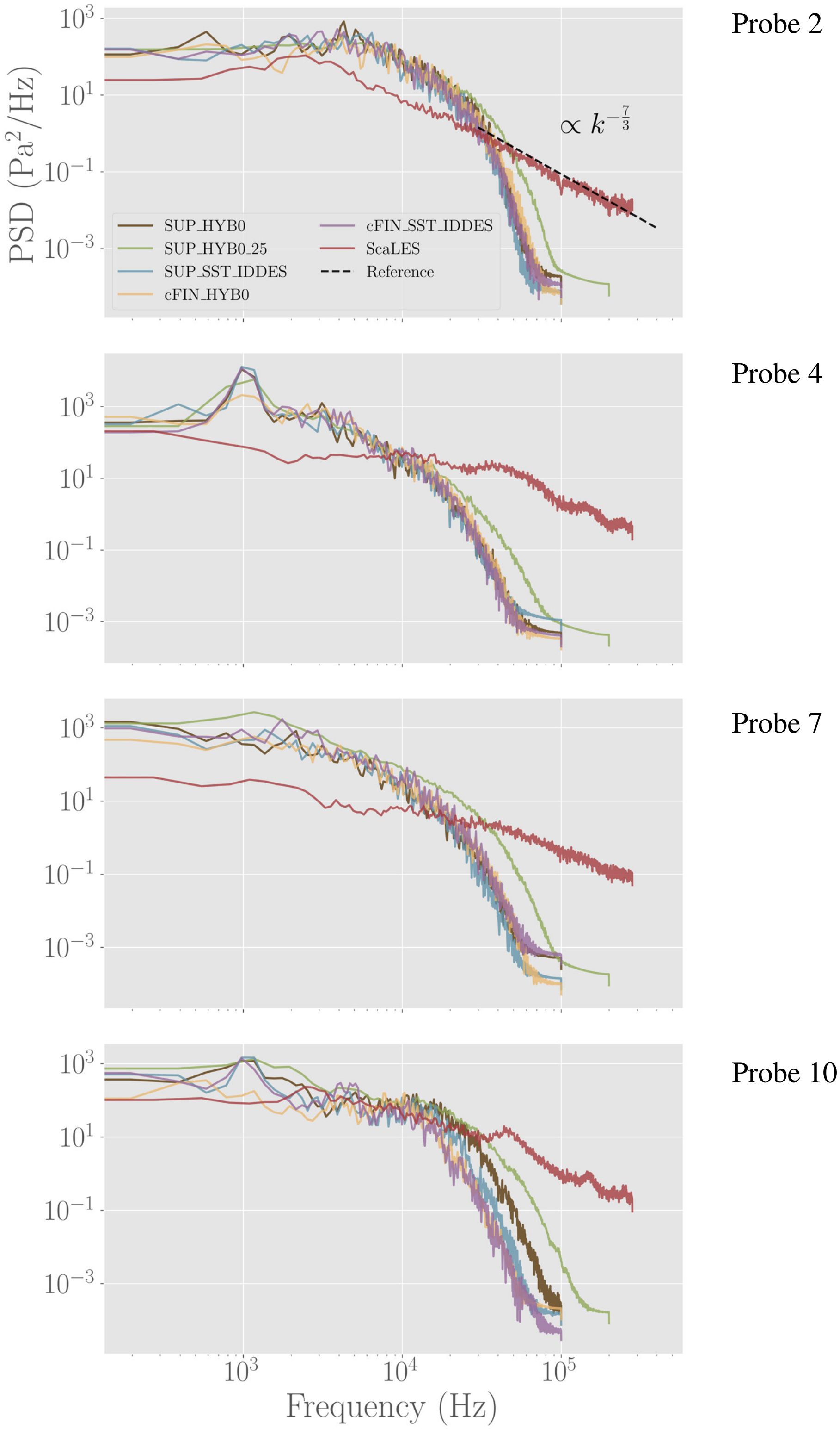

Fig. 13 Pressure power spectral density spectra at the four AVT-390 probes P2, P4, P7, and P10. WMLES (red) and five other submissions are processed through identical Welch's method parameters (Hamming window, 2048-sample segments, 50% overlap; fewer when the record length forces it). The dashed black line indicates the $f^{-7/3}$ Kolmogorov scaling for the pressure spectrum [28] for orientation. Operating point $\sigma = 17.5°$.

local flow structures, which is deferred.

A handful of caveats apply to the foregoing comparison. The solver time steps differ, both studies satisfy the Nyquist criterion for the ∼ 1 kHz scale of interest, but the Nyquist frequencies are not identical. The grid topology also differs: the other AVT-390 scale-resolving simulations run on unstructured body-fitted meshes with hybrid RANS–LES wall treatments, while the present work uses a Cartesian octree mesh with an explicit equilibrium wall model. The intent of the comparison is therefore not adjudicative, but to contribute an additional observation to the task group's collective picture: two scale-resolving treatments with materially different closures producing materially different unsteady pressure spectra.

VI. Summary

Wall-modeled large eddy simulations of the DLR LK6E2 generic missile airframe have been presented over the angle-of-incidence range $13° \leq \sigma \leq 19°$ at $M_\infty = 0.85$, $\lambda = 45°$, extending the sweep of [10]. The campaign addresses two objectives set by the AVT-390 task group: quantitative comparison of the integrated rolling moment against the DLR HST/TWG wind-tunnel envelope, and comparison of unsteady surface pressure at numerical probes against the scale-resolving simulations of Tormalm *et al.* [8].

Integrated loads and the two breaks. The $C_l(\sigma)$ curve produced by the present WMLES tracks the HST/TWG wind-tunnel envelope across the full sampled range. Both breaks in the rolling-moment curve are resolved: the primary break near $\sigma \approx 16°$, recovered at the same fidelity reported in [10], and a secondary, weaker break near $\sigma \approx 14°$ that had been observed in the wind tunnel but not previously sampled at sufficient resolution in CFD. A common mechanism is proposed for the two features: progressive weakening and eventual disappearance of the leading normal shock on Wing 4 as σ increases, accompanied by growth of an outboard separated region and reorganization of the Wing 4 vortex system. A per-wing decomposition shows that the kink in the integrated rolling moment is concentrated on Wing 4 between $\sigma = 13.5°$ and $14.5°$ while the Wing 2, Wing 1, and Wing 3 slopes remain essentially constant.

Probe pressure spectra. At the matching probe locations and the common operating point ($\sigma = 17.5°$, $\lambda = 45°$, $M_\infty = 0.85$), the present WMLES probe spectra are compared with the hybrid RANS–LES results of [8] on a same-pipeline basis using raw probe pressure traces from five additional scale-resolving submissions. The dominant peak in the 1 kHz band identified by [8] is present in the WMLES at the same probes, with the energy distributed over a broader frequency band rather than concentrated in a narrowband peak. At the Wing 3 / body-junction probe (P2) the WMLES decay above the peak is approximately $f^{-7/3}$, in the Kolmogorov-scaling range for the pressure spectrum in locally isotropic turbulence [28]; the other submissions show steeper decays at the same probe consistent with the damping out scales above the resolved-modeled crossover. At other separated-flow probes the WMLES decays are shallower than Kolmogorov, suggesting that shock-induced unsteadiness or wall-bounded contributions overlay the inertial range there. The dominant peak frequency in the WMLES varies across probe locations (∼ 0.4 kHz at P4, ∼ 0.5 kHz at P7, ∼ 2 kHz at P2, ∼ 2.9 kHz at P10), in contrast to the more nearly-uniform 1 kHz peak the other submissions display across most probes.

Scope and caveats. The physical interpretation of the secondary break put forward here rests on a small number of angles in the 13°–15° range and on the per-wing decomposition of mean loads; longer integration windows at those angles would tighten the slope estimates and strengthen the attribution of the kink to Wing 4. The scale-resolving treatment makes the dependence on turbulence-model closure implicit to the sub-grid model, side-stepping the compressibility-correction sensitivity documented for RANS approaches in the present special session [11]; this does not adjudicate among the RANS closure variants examined there, but it does remove that source of uncertainty from the present results. The cross-method PSD comparison is non-adjudicative: the reference submissions and the present WMLES use different mesh topologies and wall treatments. The intent of the present results is to contribute an additional data point to the AVT-390 collective picture rather than to rank methods.

Acknowledgments

The authors thank the NATO Science and Technology Organization Applied Vehicle Technology panel Task Group AVT-390 members: (in alphabetical order, by organization) Daniel Lesieutre (AMA Inc.), Fahri Erinç Hızır and Tolga Köktürk (Aselsan Inc.), Michael Anderson (Corvid Technologies), Michel Visonneau (ECN/CNRS), Christian Schnepf

(German Aerospace Center, DLR), Magnus Tormalm (Swedish Defense Research Agency, FOI), Gaëtan Loupy (MBDA France), Nigel Taylor (MBDA UK), Andrea Rausa and Alberto Guardone (Politecnico di Milano), Erdem Dikbaş (Roketsan Inc.), Vicente Romero (Sandia National Laboratories), and James DeSpirito (U.S. Army Research Laboratory). Also, the German Aerospace Center (DLR) for providing the LK6E2 geometry and the HST and TWG wind-tunnel measurements used for validation.

References

[1] Taylor, N. J., et al., "AVT-316: Overview of the NATO STO Research Programme on Vortex Interaction Effects Relevant to Military Air Vehicle Performance," *AIAA SciTech 2022 Forum*, 2022.

[2] Taylor, N. J., et al., "AVT-316: Prediction of Vortex Interactions on a Generic Missile Configuration," *AIAA SciTech 2022 Forum*, 2022.

[3] Schnepf, C., et al., "DLR LK6E2 Wind Tunnel Experiments and Data Set Description," *AIAA SciTech 2022 Forum*, 2022.

[4] DeSpirito, J., et al., "RANS Predictions on the DLR LK6E2," *AIAA SciTech 2022 Forum*, 2022.

[5] Taylor, N. J., "AVT-390: Overview of the Principal Outcomes for the DLR LK6E2 Airframe," *AIAA AVIATION FORUM AND ASCEND*, 2024. https://doi.org/10.2514/6.2024-4242.

[6] Schnepf, C., Schülein, E., Weiss, S., and Henne, U., "Additional Wind Tunnel Data for the Transonic LK6E2 Missile Airframe," *AIAA AVIATION FORUM AND ASCEND*, 2024. https://doi.org/10.2514/6.2024-4238.

[7] Anderson, M., Schnepf, C., Dikbas, E., Tormalm, M. H., DeSpirito, J., Loupy, G., and Rausa, A., "Further Comparisons of Predicted and Measured Aerodynamic Characteristics of the DLR LK6E2 Missile Airframe (RANS)," *AIAA AVIATION FORUM AND ASCEND*, 2024. https://doi.org/10.2514/6.2024-4239.

[8] Tormalm, M. H., DeSpirito, J., Schnepf, C., Dikbas, E., and Anderson, M., "Further Comparisons of Predicted and Measured Aerodynamic Characteristics of the DLR LK6E2 Missile Airframe (Scale Resolving)," *AIAA AVIATION FORUM AND ASCEND*, 2024. https://doi.org/10.2514/6.2024-4240.

[9] Guardone, A., and Rausa, A., "AVT-390: Outlook on Innovative Simulation Technologies Arising from Analyses of the DLR LK6E2," *AIAA AVIATION 2024 Forum*, 2024.

[10] Angel, J. B., Ghate, A. S., Kenway, G. K. W., Wong, M. L., and Kiris, C. C., "DLR LK6E2 Missile Airframe Validation Study Using Wall-Modeled Large Eddy Simulations," *AIAA SCITECH 2025 Forum*, 2025, p. 1949.

[11] Rausa, A., Guardone, A., Anderson, M., Schnepf, C., Tormalm, M. H., Dikbaş, E., DeSpirito, J., and Loupy, G., "The Influence of Compressibility Corrections on RANS Computations of the DLR LK6E2 Missile Airframe," *AIAA AVIATION 2026 Forum*, 2026.

[12] Dikbaş, E., Loupy, G., et al., "Anisotropic Adaptive Mesh Refinement for RANS Computations of the DLR LK6E2 Missile Airframe," *AIAA AVIATION 2026 Forum*, 2026.

[13] Moin, P., Squires, K., Cabot, W., and Lee, S., "A dynamic subgrid-scale model for compressible turbulence and scalar transport," *Physics of Fluids A: Fluid Dynamics*, Vol. 3, No. 11, 1991, pp. 2746–2757.

[14] Lilly, D., "A proposed modification of the Germano subgrid-scale closure method," *Phys Fluids A*, Vol. 4, 1992, pp. 633–635.

[15] Shu, C.-W., and Osher, S., "Efficient implementation of essentially non-oscillatory shock-capturing schemes," *Journal of Computational Physics*, Vol. 77, No. 2, 1988, pp. 439–471.

[16] Gottlieb, S., and Shu, C.-W., "Total variation diminishing Runge-Kutta schemes," *Mathematics of computation*, Vol. 67, No. 221, 1998, pp. 73–85.

[17] Gottlieb, S., Shu, C.-W., and Tadmor, E., "Strong stability-preserving high-order time discretization methods," *SIAM Review*, Vol. 43, No. 1, 2001, pp. 89–112.

[18] Kenway, G. K., Ghate, A., Browne, O. M., Wong, M. L., Angel, J. B., and Kiris, C. C., "Immersed Boundary Wall-Modelled Large Eddy Simulations of a Generic Hammerhead Payload Fairing," *AIAA AVIATION FORUM AND ASCEND 2024*, 2024, p. 3693.

[19] Ghate, A. S., Angel, J. B., Kenway, G., Wong, M. L., and Kiris, C. C., "Large Eddy Simulations of High-Lift Common Research Model in the NTF Wind Tunnel at Flight Scale Reynolds Numbers," *AIAA SCITECH 2026 Forum*, 2026, p. 0020.

[20] Wong, M. L., Ghate, A., Kenway, G. K., Angel, J. B., and Kiris, C. C., "Immersed Boundary Wall-Modelled Large Eddy Simulations of Straight Wings with Three-Dimensional Ice Accretion," *AIAA AVIATION FORUM AND ASCEND 2024*, 2024, p. 4000.

[21] Wong, M. L., Ghate, A., Kenway, G. K., Angel, J. B., and Kiris, C. C., "Immersed Boundary Wall-Modelled Large Eddy Simulations of Subsonic Jet Flows and Acoustics," *AIAA AVIATION FORUM AND ASCEND 2024*, 2024, p. 4466.

[22] Angel, J. B., Wong, M. L., Kenway, G., Ghate, A., and Kiris, C. C., "Validation of Immersed Boundary Wall-Modelled Large Eddy Simulations with F-16XL Flight Data," *AIAA AVIATION FORUM AND ASCEND 2024*, 2024, p. 4374.

[23] Angel, J. B., Ghate, A., Kenway, G., Wong, M. L., Kiris, C. C., and Ashton, N., "Immersed boundary wall-modelled large eddy simulations for automotive aerodynamics," *AIAA Aviation Forum and Ascend 2024*, 2024, p. 4172.

[24] Ghate, A. S., Wong, M. L., Kenway, G., Angel, J. B., Kiris, E., and Kiris, C. C., "Noise Prediction of Ducted Fans using Immersed Boundary Wall-Modeled Large Eddy Simulations," *32nd AIAA/CEAS Aeroacoustics Conference (2026)*, 2026.

[25] Wong, M. L., Ghate, A. S., Kenway, G., Angel, J. B., Kiris, E., and Kiris, C. C., "Counter-Rotating Open Rotor Noise Predictions Using Immersed Boundary Wall-Modeled Large Eddy Simulation," *32nd AIAA/CEAS Aeroacoustics Conference (2026)*, 2026.

[26] Flyvbjerg, H., and Petersen, H. G., "Error estimates on averages of correlated data," *The Journal of Chemical Physics*, Vol. 91, No. 1, 1989, pp. 461–466. https://doi.org/10.1063/1.457480.

[27] Welch, P. D., "The use of fast Fourier transform for the estimation of power spectra: a method based on time averaging over short, modified periodograms," *IEEE Transactions on Audio and Electroacoustics*, Vol. 15, No. 2, 1967, pp. 70–73. https://doi.org/10.1109/TAU.1967.1161901.

[28] George, W. K., Beuther, P. D., and Arndt, R. E. A., "Pressure spectra in turbulent free shear flows," *Journal of Fluid Mechanics*, Vol. 148, 1984, pp. 155–191. https://doi.org/10.1017/S0022112084002299.